Magn Reson Mater Phy (2008) 21:53–61
DOI 10.1007/s10334-007-0100-4

RESEARCH ARTICLE

# Comparison of three commercially available radio frequency coils for human brain imaging at 3 Tesla

**Ralf Mekle · Wietske van der Zwaag · Andreas Joosten · Rolf Gruetter**

Received: 20 July 2007 / Revised: 4 December 2007 / Accepted: 5 December 2007 / Published online: 10 January 2008


**Abstract**
*Objective* To evaluate a transverse electromagnetic (TEM), a circularly polarized (CP) (birdcage), and a 12-channel phased array head coil at the clinical field strength of $B_0 = 3\,\mathrm{T}$ in terms of signal-to-noise ratio (SNR), signal homogeneity, and maps of the effective flip angle $\alpha$.
*Materials and methods* SNR measurements were performed on low flip angle gradient echo images. In addition, flip angle maps were generated for $\alpha_{\mathrm{nominal}} = 30°$ using the double angle method. These evaluation steps were performed on phantom and human brain data acquired with each coil. Moreover, the signal intensity variation was computed for phantom data using five different regions of interest.
*Results* In terms of SNR, the TEM coil performs slightly better than the CP coil, but is second to the smaller 12-channel coil for human data. As expected, both the TEM and the CP coils show superior image intensity homogeneity than the 12-channel coil, and achieve larger mean effective flip angles than the combination of body and 12-channel coil with reduced radio frequency power deposition.
*Conclusion* At 3 T the benefits of TEM coil design over conventional lumped element(s) coil design start to emerge, though the phased array coil retains an advantage with respect to SNR performance.

**Keywords** RF-coil · TEM coil · High field MRI · SNR · $B_1$ field

R. Mekle (✉) · W. van der Zwaag · R. Gruetter
Centre d'Imagerie BioMedicale (CIBM),
Ecole Polytechnique Federale de Lausanne (EPFL),
EPFL SB IPMC LIFMET, CH F0 572 (Batiment CH),
Station 6, 1015 Lausanne, Switzerland
e-mail: ralf.mekle@epfl.ch

R. Mekle · W. van der Zwaag · A. Joosten · R. Gruetter
Laboratory for Functional and Metabolic Imaging (LIFMET),
Ecole Polytechnique Federale de Lausanne (EPFL),
Lausanne, Switzerland

R. Mekle · W. van der Zwaag
Department of Radiology, University of Lausanne,
Lausanne, Switzerland

R. Gruetter
Departments of Radiology,
Universities of Lausanne and Geneva,
Lausanne/Geneva, Switzerland

## Introduction

Three Tesla (T) magnetic resonance imaging (MRI) scanners have been installed as valuable clinical and research tools. Advantages of performing nuclear magnetic resonance (NMR) experiments at high main magnetic field strengths $B_0 (\geq 3\,\mathrm{T})$ include enhanced sensitivity for all NMR techniques in general and a larger chemical shift dispersion for magnetic resonance spectroscopy (MRS) in particular. On the other hand, wave phenomena due to shortened radio frequency (RF)-wavelengths, e.g., geometric interference phenomena, lead to inhomogeneous $B_1$ field distributions and thus distorted image intensities [1]. In addition, conventional lumped element(s) coil designs suffer from non-uniform current distributions, decreased conductor skin depths, self-resonance below the desired frequency of operation, and increased electromagnetic radiation losses [2]. To exploit the inherent advantages and to overcome the challenges of the use of high field scanners for MRI/MRS, dedicated RF-coils, such as transverse electromagnetic (TEM) [2] and microstrip transmission line volume coils [3] have been developed. In principle, the TEM coil is a transmission line tuned coaxial cavity resonant in a TEM mode. As such it develops the necessary RF-field using "distributed" (transmission line) elements rather than lumped or discrete components [2,4].

As a result, the TEM coil has the potential of being more efficient at higher frequencies. Both types of coils, TEM and microstrip transmission line, have been successfully utilized at $B_0 \geq 4\,\mathrm{T}$ [5–7]. Other commonly used RF probes include the birdcage coil [8] and the phased array coil [9]. The birdcage resonator is based on the concept that, if wavelength effects can be neglected, a perfectly homogeneous $B_1$ field can be generated within an infinitely long cylinder, on which surface currents parallel to the axis of the cylinder and proportional to the sine of the azimuthal angle are imprinted. This type of RF probe has long been the clinical workhorse at 1.5 T [8], but has been used on 3 T systems as well [10]. Phased array coils were originally developed to exploit the high signal-to-noise ratio (SNR) of surface coils for volumetric imaging [9]. More recently, the array design found renewed interest, because of parallel imaging techniques that allow acceleration of image acquisition [11].

While comparisons of the TEM coil with other coil types have been carried out using simulations [12–14], benchmark tests [15], and research dedicated high field scanners [4,16], the authors are not aware of any published experimental coil comparison studies at the clinically relevant field strength of $B_0 = 3\,\mathrm{T}$. Moreover, in large MRI centers multiple commercial RF-coils designed for human brain imaging might be available. Therefore, the aim of this study was to compare a TEM, a circularly polarized (CP) (birdcage), and a 12-channel phased array head coil on a clinical 3 T MRI system and to provide experimental data that aid in coil selection. In this study, coil sensitivity and signal homogeneity were assessed by measuring the SNR and the signal intensity variation (SIV), respectively. In addition, maps of the effective flip angle $\alpha$, which provide a measure for the homogeneity of the RF-excitation field $B_1^+$ [17], were generated.

## Materials and methods

All scans were performed on a 3 T Trio TIM system (Siemens Medical Solutions, Erlangen, Germany). The following commercially available head coils were included in this study: a TEM coil (transmit (Tx)/receive (Rx), MR Instruments Inc., MN, USA) with dimensions (length($L$) × width($W$) × height($H$)) = $38 \times 35 \times 35\,\mathrm{cm}^3$, inside diameter (ID) = 26.5 cm, inside depth ($I_{\mathrm{Depth}}$, i.e., from the back closed wall to the front open wall) = 22 cm, and 16 resonant elements; a CP (birdcage) coil (Tx/Rx) with $L \times W \times H = 43 \times 37 \times 37\,\mathrm{cm}^3$, ID = 26.5 cm, $I_{\mathrm{Depth}} = 33\,\mathrm{cm}$, and 16 rungs; and a 12-channel phased array (Rx only) with $L \times W \times H = 30 \times 30 \times 33\,\mathrm{cm}^3$, ID = 25 cm, $I_{\mathrm{Depth}} = 27\,\mathrm{cm}$, and one ring of 12 elements, where elements are 8 cm wide and 6.5 cm spaced apart (the latter two coils by Siemens Medical Solutions, Erlangen, Germany). All three coils were tuned for human head imaging.

### Signal-to-noise ratio (SNR) and signal intensity variation (SIV) measurements

The methodology for the SNR and SIV measurements was based on the experiments described in [7] and is briefly reviewed in the following sections.

#### *Phantom studies*

A 15 cm diameter cylindrical bottle with overall length of 24 cm filled with vegetable oil was used as a phantom. The oil was chosen for its low relative permittivity ($\varepsilon_r \sim 3$–4). Initially, sagittal gradient recalled echo (GRE) images across the center of the oil phantom, which was positioned as close to isocenter as possible, were acquired with the following scan parameters: TR/TE = 2000/3.8, matrix size = 256 × 256, square FOV = 240 mm, slice thickness = 5 mm, $\alpha = 10°$, BW = 260 Hz/pixel, and NA = 1. From these images a 1D intensity profile through the center of the phantom was used to define the slice position, which showed the strongest MR signal intensity along the $z$-axis (see Fig. 1). At this position a transversal slice was acquired using a GRE sequence with the same scan parameters, except for a modified TR (TR = 5000 ms) to minimize saturation effects.

The SNR was measured in five different regions-of-interest (ROIs) in the transversal slices (as shown in Fig. 2). Signal was measured as average magnitude image intensity in each ROI ($\mathrm{SI_{ROI}}$). Noise was estimated as standard deviation (SD) of image intensity in a ROI located outside the phantom, $\sigma_{\mathrm{Noise}}$. The SNR was then computed as $\mathrm{SI_{ROI}}/\sigma_{\mathrm{Noise}}$. To assess image homogeneity, SIV across the slice was calculated as $\mathrm{SIV} = (|\mathrm{SI_C} - \mathrm{ASI_p}|/\mathrm{ASI_a}) \times 100\%$, where $\mathrm{SI_C}$ is the image intensity in the center ROI, and $\mathrm{ASI_p}$ and $\mathrm{ASI_a}$ are the average image intensities of the four peripheral and of all five ROIs, respectively.

#### *Human brain studies*

The SNR was measured on transversal GRE images of five human volunteers acquired with the same scan parameters as used for the phantom, except for TR = 2000 ms and matrix size = 128 × 128 to reduce scan time. For the human head scans, coil positioning was adapted so that for each subject the same anatomy was imaged at the most sensitive location along the $z$-axis of each coil as determined previously. Measurements from all subjects were averaged for each ROI. In addition, SNR maps were generated by dividing each spatially smoothed (applying a 5 × 5 median filter kernel) GRE image by the previously estimated noise value [16]. The SNR maps were evaluated as color scale images, and SNR profiles through the center of the brain along the posterior–anterior direction were extracted from the SNR maps.

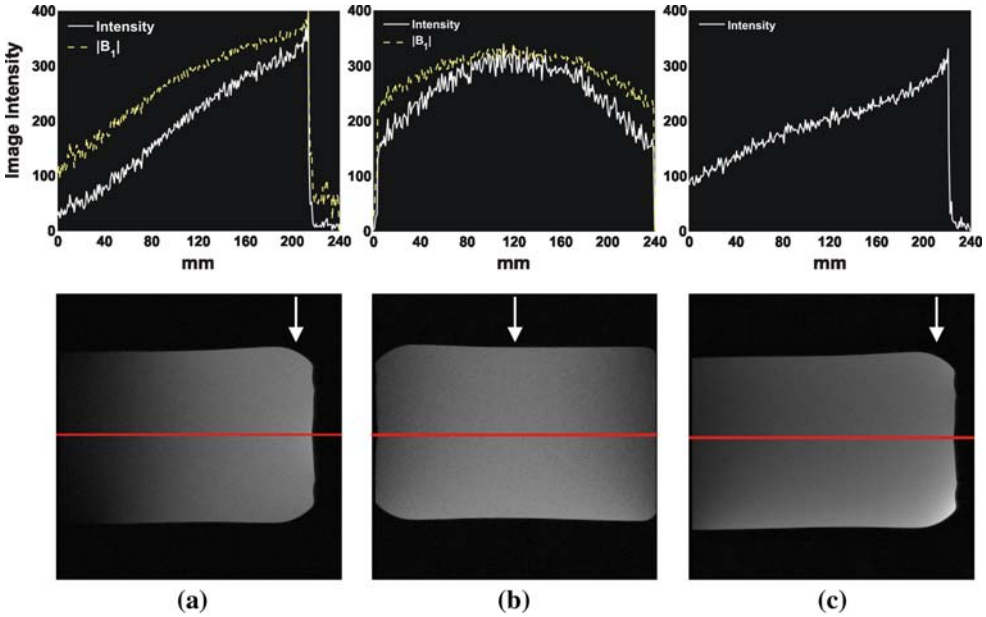


**Fig. 1** Sagittal GRE images of the oil phantom (*lower row*) and their corresponding 1D intensity profiles (*upper row*) for the **a** TEM coil, **b** CP coil, and **c** 12-channel phased array coil. For each coil a 1D profile through the center of the phantom was used to define the slice position, which showed the strongest MR signal intensity (most sensitive region) along the $z$-axis. *Arrows* indicate the respective locations of the transversal slices used for SNR measurements and shown in Fig. 2

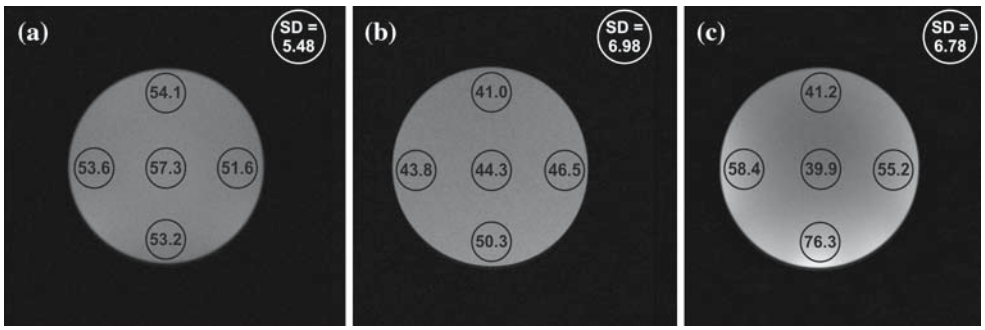


**Fig. 2** Transversal GRE images of the oil phantom acquired with **a** TEM coil, **b** CP coil, and **c** 12-channel phased array coil. SNR values are shown in *black* in each ROI. The standard deviation (SD) of the noise, $\sigma_{\text{Noise}}$, is given in *white* in the noise ROI. The same window leveling setting was applied to all three images. Note the increased image intensity variations in **c** compared to the images in **a** and **b**

All acquisitions were repeated for each coil and magnitude images were reconstructed. No image intensity correction was applied for any of the coils. Experimental parameters, including positioning, were kept the same throughout the entire evaluation.

## Flip angle ($B_1^+$) mapping

To assess the homogeneity of the RF-excitation field $B_1^+$ of each coil, maps of the flip angle $\alpha$ were generated using the double angle method [18,19]. In this technique, two GRE or spin echo (SE) images are acquired using identical scan parameters, but different flip angles $\alpha_1$ and $\alpha_2$. For GRE images and when using sufficiently long repetition times (TR $\geq 5\,T_1$), and choosing $\alpha_2 = 2\alpha_1$, the flip angle $\alpha$ can be computed as [18,19]:

$$\alpha(i,\,j) = \arccos\left(\frac{I_2(i,\,j)}{2I_1(i,\,j)}\right) \tag{1}$$

where $I_1(i,\,j)$ and $I_2(i,\,j)$ are the image intensities at pixel locations $(i,\,j)$ of image 1 and 2, respectively.

### *Phantom studies*

Transversal GRE images were acquired using the following scan parameters: TR/TE = 5000/3.8, matrix size = 256×208,

FOV = 240 × 196 mm$^2$, slice thickness = 5 mm, BW = 260 Hz/pixel, and NA = 1. Flip angles $\alpha_1 = 30°$ and $\alpha_2 = 60°$ were chosen yielding flip angle maps for a nominal $\alpha = 30°$. Prior to flip angle computation, images were thresholded to exclude pixels outside of the object (phantom) and smoothed using a median filter with a kernel of 5 by 5 to reduce noise contributions. Flip angle maps were then calculated by applying Eq. [1] to all pixels in the image.

*Human brain studies*

To shorten the scan time, the matrix size was reduced to 128 × 104 for the human brain measurements. All other scan parameters were identical to those used for the phantom. To obtain similar coil loading conditions, in each coil the head was positioned the same way as during regular brain examinations. Prior to thresholding and filtering, the two human brain datasets of each subject were coregistered using FLIRT (FSL, [20]) to minimize potential subject motion effects. Any remaining pixels with $I_2 > 2 \cdot I_1$ were set to zero, as these yield complex values in the flip angle maps. Such pixels were only found in the vicinity of the scull attributed to low SNR. The remaining processing steps were the same as for the phantom. Flip angle mapping was performed for five subjects, and resulting values for $\alpha$ were averaged.

## Results

Signal-to-noise ratio (SNR) and signal intensity variation (SIV) measurements

*Phantom studies*

As seen from the sagittal GRE images of the oil phantom and their corresponding 1D intensity profiles shown in Fig. 1, the TEM and the 12-channel coil had their most sensitive region along the $z$-axis towards their superior end, whereas the coil center was most sensitive for the CP coil (see Fig. 1b). This was attributed to the fact that the former two coils are closed with an end plate, while the CP coil is open at both ends. Note that for the chosen scan parameters and sequence, image intensity is proportional to $|B_1|^2$ for the TEM and CP coils ($|B_1|$ profiles are indicated by yellow dashed lines in Fig. 1a, b), since these coils are used for both transmission and reception. This proportionality is only valid, when small flip angles are used (as was the case in this study) and when the RF-wavelength $\lambda$ can be considered to be approximately constant over the sample, which at 3 T for the oil phantom still holds ($\lambda \sim 1.2$–$1.35$ m). Otherwise, signal intensity depends on the (complex) excitation field $B_1^+$ and reception field $B_1^-$ [17]. In contrast, since the 12-channel array coil was only used for signal reception, this proportionality does not hold. In images acquired with the latter, a substantial intensity gradient along the transverse direction was observed, which was absent (TEM coil) or only minor (CP coil) in results obtained with the other two coils. This observation was qualitatively and quantitatively confirmed by the phantom data shown in Fig. 2. From top to bottom in the transversal slices, SNR increased strongly for the 12-channel, slightly for the CP, and remained almost constant for the TEM coil. For the latter, SNR was only slightly elevated in the center (see Fig. 2a). The increased image intensity variation across the transversal slice for the 12-channel coil was reflected by the larger SIV = 33%. SIV was fourfold reduced (between 2 and 8%) for the CP and TEM coil images corroborating the visual observation of increased image intensity homogeneity. Noise ($\sigma_{\text{Noise}}$) was lowest in phantom data acquired with the TEM coil and highest in data obtained with the CP coil. In all peripheral ROIs, the lowest SNR was measured using the CP coil. The highest SNR for the three lower peripheral ROIs was obtained with the 12-channel array, and for the upper peripheral and central ROIs with the TEM coil. Mean SNR values (averaged over all five ROIs) for the phantom images in Fig. 2 are given in Table 1. Differences in mean SNR between coils were 19.5% (TEM − CP), 20% (12 channel − CP), and 0.4% (12 channel − TEM). However, differences in SNR measured in individual ROIs ranged from 0.5 up to 52%.

*Human brain studies*

Transversal GRE human brain images from a single representative volunteer acquired with all RF-probes are presented in Fig. 3 together with the corresponding SNR maps. As can be seen from Fig. 3a–c, excellent image quality was achieved with all three coils. Image intensity variations for the 12-channel array coil were visually somewhat less pronounced in Fig. 3c than for phantom images. Mean values and standard deviations of the SNR and $\sigma_{\text{Noise}}$ measured in human brain images ($N = 5$ subjects) are shown in Table 1 for all three coils. As shown in Table 1 and as opposed to the results from the phantom studies, the highest SNR for all ROIs was found using the 12-channel coil. The differences in SNR for the central and most superior ROIs between the TEM and 12-channel probes were less than 10% though. Images acquired with the CP coil yielded the lowest SNR for the superior four ROIs. Only the SNR in the most inferior ROI was fractionally lower in the image acquired with the TEM coil. Noise was lowest in human brain data obtained with the TEM and highest in data measured with the CP coil. Mean SNR values (averaged over all five ROIs) for the human brain data are also included in Table 1. Differences in mean SNR between coils were 11% (TEM − CP), 37% (12 channel − CP), and 24% (12 channel − TEM). However, differences in SNR measured in individual ROIs ranged from 2 up to 59%.

**Table 1** Mean values averaged over $N = 5$ human subjects and their standard deviations for the SNR and $\sigma_{\text{Noise}}$ for all three coils computed for the ROIs of transversal GRE images shown in Fig. 3

| | Oil phantom | Human brain | | | | | | |
|---|---|---|---|---|---|---|---|---|
| Coil | Mean SNR[a] | Mean SNR[a] | ROI 1 | ROI 2 | ROI 3 | ROI 4 | ROI 5 | $\sigma_{\text{Noise}}$ |
| TEM | $54.0 \pm 2.08$ | $134 \pm 15.1$ | $158 \pm 15.7$ | $140 \pm 11.6$ | $122 \pm 13.2$ | $125 \pm 10.2$ | $125 \pm 14.5$ | $2.15 \pm 0.03$ |
| CP | $45.2 \pm 3.45$ | $121 \pm 13.5$ | $141 \pm 22.5$ | $108 \pm 16.2$ | $115 \pm 19.0$ | $128 \pm 21.8$ | $111 \pm 19.8$ | $2.92 \pm 0.22$ |
| 12 Channel array | $54.2 \pm 14.84$ | $166 \pm 20.9$ | $171 \pm 22.5$ | $151 \pm 17.7$ | $148 \pm 18.1$ | $200 \pm 22.2$ | $159 \pm 24.2$ | $2.72 \pm 0.28$ |

The location of the ROIs in the GRE images is indicated in the inset below. Mean SNR values averaged over all five ROIs for oil phantom and human brain data are also included

[a] Averaged over all five ROIs

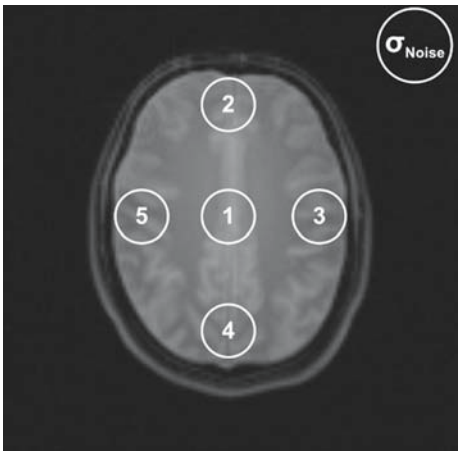


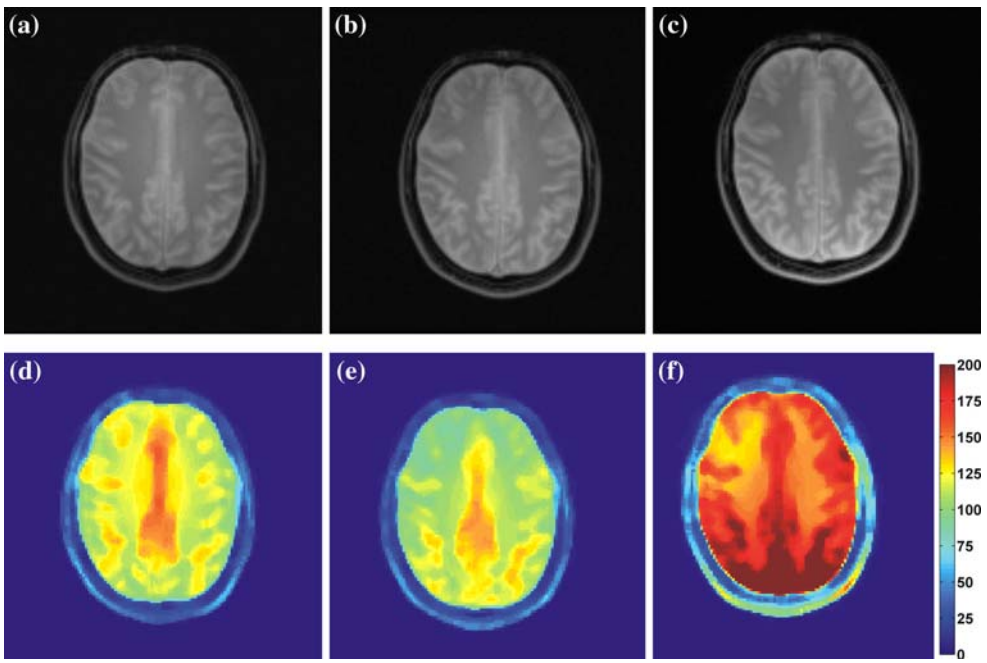


**Fig. 3** Transversal GRE brain images from a single representative human volunteer acquired with **a** TEM coil, **b** CP coil, and **c** 12-channel phased array coil. Individual window leveling settings were applied to each image. Corresponding SNR maps of the spatially smoothed GRE images are shown in **d**–**f**. All maps are created with the same color scale for comparison. Note the increased SNR achieved with the 12-channel array, especially in the inferior part of the brain, where the coil elements are closest to the head

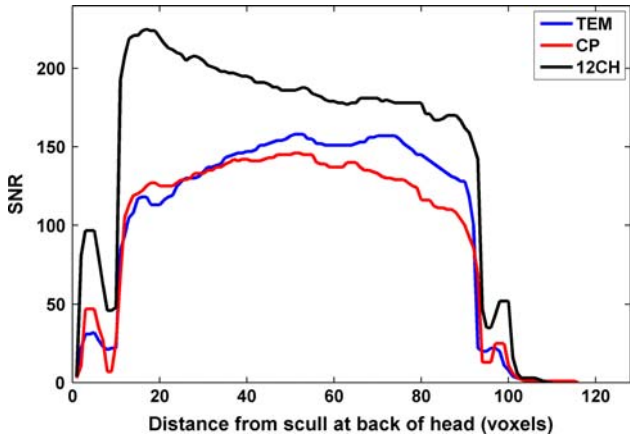


**Fig. 4** SNR profiles through the center of the brain along the posterior–anterior direction obtained from the SNR maps shown in Fig. 3 for all three RF coils. The profiles nicely illustrate the quantitative results for the different ROIs along the center of the brain presented in Table 1

The SNR maps shown in Fig. 3d–f that were generated from the GRE images in Fig. 3a–c as well as the SNR profiles presented in Fig. 4 illustrate these quantitative results very well. Note the increased SNR obtained with the 12-channel coil, especially in the inferior part of the brain, where the coil elements are closest to the head and thus locally receive the highest signal.

Flip angle ($B_1^+$) mapping

Note that flip angle ($B_1^+$) maps presented for the 12-channel coil are actually flip angle maps for the body coil, since in this case, transmission is performed with the body coil. For the sake of simplicity in this comparison, it is still referred to as flip angle map of the 12-channel coil.

*Phantom studies*

Maps of the flip angle $\alpha$ for the nominal flip angle $\alpha_{\text{nominal}} = 30°$ in the oil phantom for all three coils are shown in Fig. 5. All maps are largely homogeneous. As seen in Fig. 5, using the phantom as a load, flip angles achieved were smaller than $\alpha_{\text{nominal}}$ for all three coils. Overall, highest flip angles were attained with the TEM and the CP coils, and lowest values for $\alpha$ were calculated for the 12-channel coil. Minimum, maximum, and mean values of the effective flip angle in the oil phantom achieved with the three coils are listed in Table 2.

*Human brain studies*

In all cases, subject motion between acquired scans was small (<1 pixel). Resulting flip angle maps for $\alpha_{\text{nominal}} = 30°$ from human brain scans of a single representative volunteer for all

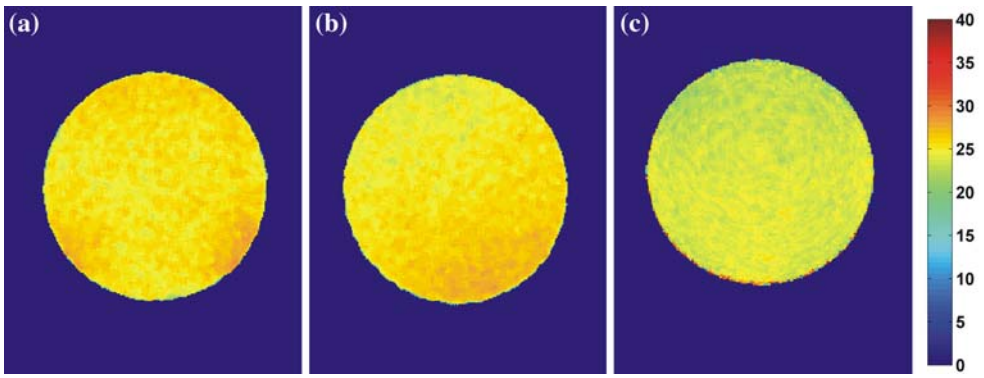


**Fig. 5** Maps of the effective flip angle for $\alpha_{\text{nominal}} = 30°$ in the oil phantom for **a** TEM coil, **b** CP coil, and **c** 12-channel phased array coil (body coil). Maps were thresholded and median filtered with a $5 \times 5$ kernel. Larger effective flip angles were obtained with the TEM and CP coils compared to the 12-channel phased array coil

**Table 2** Values for minimum ($\alpha_{\text{min}}$), maximum ($\alpha_{\text{max}}$), mean ($\mu_\alpha$), and standard deviation ($\sigma_\alpha$) for the effective flip angle $\alpha$ for $\alpha_{\text{nominal}} = 30°$ for the flip angle maps generated for all coils from phantom and human brain data

| Coil | Oil phantom | | | | Human brain | | | |
|---|---|---|---|---|---|---|---|---|
| | $\alpha_{\text{min}}$ (°) | $\alpha_{\text{max}}$ (°) | $\mu_\alpha$ (°) | $\sigma_\alpha$ (°) | $\alpha_{\text{min}}$ (°)[a] | $\alpha_{\text{max}}$ (°)[a] | $\mu_\alpha$ (°) | $\sigma_\alpha$ (°)[a] |
| TEM | 23.2 | 28.5 | 25.6 | 0.7 | $19.6 \pm 2.7$ | $34.1 \pm 1.8$ | $27.9 \pm 1.0$ | $1.9 \pm 0.2$ |
| CP | 22.5 | 28.6 | 25.6 | 0.9 | $17.6 \pm 1.0$ | $32.3 \pm 1.6$ | $26.0 \pm 0.5$ | $2.0 \pm 0.4$ |
| 12 Channel array (body) | 19.7 | 25.9 | 23.7 | 0.7 | $12.5 \pm 6.6$ | $31.8 \pm 2.0$ | $23.9 \pm 0.9$ | $2.4 \pm 0.3$ |

Human data are given as mean values together with their standard deviations after averaging over $N = 5$ subjects
[a] Averaged over $N = 5$ subjects

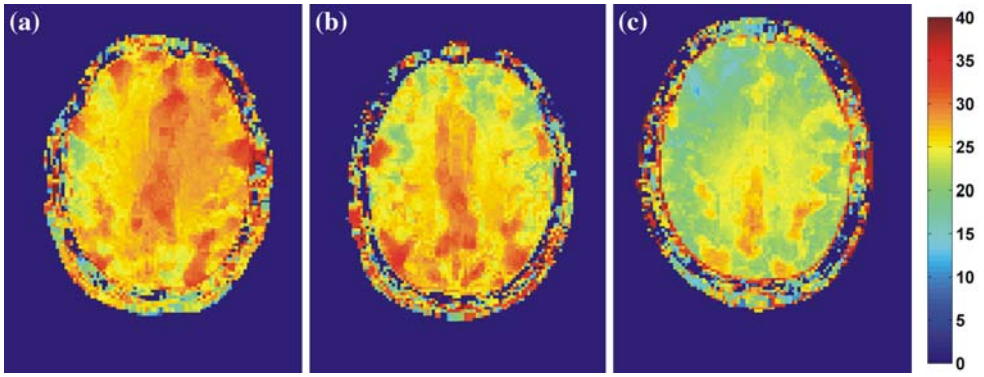


**Fig. 6** Maps of the effective flip angle for $\alpha_{\text{nominal}} = 30°$ in human brain of a single representative volunteer for **a** TEM coil, **b** CP coil, and **c** 12-channel phased array coil (body coil). Maps were motion corrected, thresholded, and median filtered with a $5 \times 5$ kernel. Similar to the results from phantom experiments shown in Fig. 5, larger effective flip angles were achieved employing either of the two Tx/Rx coils compared to the combination of body and 12-channel coil

three coils are presented in Fig. 6. Results were very similar across all other subjects. Mean values and standard deviations for minimum, maximum, mean, and standard deviation of the effective flip angle in human brain ($N = 5$ subjects) achieved with the three coils are also included in Table 2. Slightly larger values for $\alpha$ were achieved with the TEM coil compared to the CP probe, whereas flip angles obtained for the 12-channel coil were on average 2–4° smaller (see Table 2 and also Fig. 6). All flip angle maps exhibited the largest values for $\alpha$ in a central strip of the brain, which contains a large volume fraction of cerebrospinal fluid (CSF). Overall, structures of white matter (WM) and gray matter (GM) cannot be clearly distinguished in the maps in Fig. 6 indicating some degree of $B_1^+$ homogeneity for these tissues. Note that in human compared to phantom data increased values for $\alpha_{\text{max}}$ and slightly larger values for the mean effective flip angle $\mu_\alpha$, i.e., closer to $\alpha_{\text{nominal}}$, were obtained with all three coils.

## Discussion

Excellent homogeneity of image intensity in phantom experiments as indicated by low SIV values was observed for the TEM and CP coils. In general, homogeneity of image intensity depends on the spatial dependencies of the excitation and reception distributions of a coil that can be different at high fields [21]. For the TEM and CP coils, both distributions are largely homogeneous. This finding is supported by the corresponding flip angle maps in Fig. 5 and low standard deviations of the mean effective flip angle in Table 2. In contrast, even though excitation with the body coil yields a homogeneous flip angle distribution as well (see Fig. 5c), the substantial image intensity variations observed in Fig. 2c are induced by the locally varying Rx sensitivity of the 12-channel array coil. This is not unusual and expected, especially compared to volume coils, since phased array coils tend to have a stronger sensitivity near the surface of the object being scanned. In clinical practice, these variations are usually corrected for using coil sensitivity profiles acquired in a short pre-scan.

In general, higher SNR values were obtained with the TEM coil than with the CP coil for both phantom and human brain measurements due to lower noise contributions. The latter suggests the TEM coil has improved coil electronics (e.g., integrated pre-amplifier) compared to the CP coil. Surprisingly, for phantom data, the SNR in some of the ROIs was also higher for the TEM than for the 12-channel coil due to a lower noise level. The mean SNR for these two coils was almost the same. This is somewhat unexpected, since averaging of multi-channel data should lead to reduced noise levels. For human brain scans, noise in the 12-channel coil image was larger than for the TEM coil, but higher SNR values for the 12-channel coil demonstrated the benefits of improved signal reception using multiple coil elements.

As seen from Fig. 2 and Table 1, SNR values from human brain data for the 12-channel coil are more strongly increased compared to results from phantom experiments than for the two volume coils. This discrepancy can be largely explained by the different coil loading conditions, i.e., oil phantom or human head. All three RF probes are tuned for human head imaging and are not retuned for each specific sample. Any deviation from this "optimal" coil load will reduce coil performance. Since the multi-element phased array is more sensitive with respect to different coil loading conditions than the two volume coils, its performance is correspondingly more strongly reduced, when loaded with the oil phantom. More specifically, the diameter of the oil phantom is only 15 cm, whereas a human head along the posterior-anterior direction measures typically, at least 20 cm, i.e., the superior part of the human brain in a transversal slice is actually more closely

located to the upper coil elements than the superior edge of the oil phantom. Since the sensitivity of a surface coil element decreases with distance more rapidly than the one of a volume coil, the SNR of the superior and central ROIs from phantom scans is reduced in comparison to the SNR from human brain acquisitions using the phased array.

On the other hand, the SNR gains achieved with the 12-channel coil can partially be attributed to its overall smaller dimensions resulting in a larger filling factor compared to the two volume coils. Calculating the sensitive volume for a transversal slice as $V_{\mathrm{Coil,tra}} = \pi \cdot \mathrm{ID}^2/4 \cdot \mathrm{TH}$, where TH is the slice thickness, and taking the ratio $\mathrm{V_{Coil,tra}}$ (TEM or CP)/$\mathrm{V_{Coil,tra}}$ (12-channel) gives 1.1236, which means that the filling factor for a sample of the same size for the 12-channel coil is by 12% larger than for the two volume coils resulting in corresponding SNR gains. However, since for individual ROIs the observed increase in SNR was mostly larger, other contributing factors are indicated, such as the exact distribution of the $B_1$ field within and beyond physical coil dimensions.

In this context it should be noted that the SNR values shown for the CP coil in Table 1 benefited from a different coil loading compared to the other two coils. Recall that for these measurements, the same anatomy was positioned into the most sensitive location along the longitudinal direction of each coil. Since this location was different for the CP coil than for the other two coils, the head of the volunteer had to be slightly moved out of the coil reducing coil loading. SNR measurements in human brain images of the same anatomy showed that moving the head out of the coil resulted in an increase in mean SNR by more than 20% for the same subject (data not shown).

The double angle method assumes that relaxation effects can be neglected. At 3 T and using a TR of 5000 ms, even for CSF, which is the tissue with the longest $T_1$, the ratio $\mathrm{TR}/T_1$ is approximately 2, for which it was shown that the error in the measured flip angle map attributed to saturation effects is less than 5%, when using SE sequences [22]. However, all values for the effective flip angle were below $\alpha_{\mathrm{nominal}} = 30°$ in flip angle maps for the phantom acquired with all three coils. Increased values in the flip angle maps for human brain tissue obtained with all three probes correspond to improved flip angle adjustment for human brain compared to phantom imaging. That the mean effective flip angle for these flip angle maps was still smaller than $\alpha_{\mathrm{nominal}}$ is likely caused by imperfections of the RF-pulse calibration system on the scanner at higher field strengths. Larger flip angle values along the central strip of the brain in the maps shown in Fig. 6 are an indication of the central brightening effect resulting from RF-wave interference at 3 T [23].

Apart from the criteria used for this evaluation study, other coil characteristics may play an important role for performance evaluation as well. For example, using a dedicated Tx/Rx head coil at 3 T results in reduced whole-body RF-power deposition compared to transmitting with the body coil. This enables the acquisition of an increased number of slices in certain cases, for instance turbo spin echo protocols. In this study, the vendor supplied specific absorption rate (SAR) calculation for the human brain scans used for the SNR measurements (TR/TE = 2000/3.8, $\alpha = 10°$; all scan parameters listed in the "Materials and methods" section) yielded mean values of $8.52 \times 10^{-6}$ W/kg, $8.35 \times 10^{-6}$ W/kg, and $2.29 \times 10^{-5}$ W/kg for the TEM, the CP, and the 12-channel (body) coils, respectively. Thus, even for low flip angle GRE human brain scans the difference in SAR between the two types of coils is already approximately threefold.

Likewise, more demanding applications requiring RF-fields with large $(\gamma \cdot B_1/2\pi)$ values, e.g., MR spectroscopy techniques that employ adiabatic RF-pulses with high $B_1$ peak power to minimize chemical shift registration errors will benefit from using the TEM or the CP coil compared to the combination of body and 12-channel coil. To illustrate this, $(\gamma \cdot B_1/2\pi)$ was estimated for a transmitter voltage of 500 V using the transmitter voltages of the RF-pulses employed in the human brain scans (same coil loading). The corresponding values were 1610, 1490, and 820 Hz for the TEM, the CP, and the 12-channel (body) coils, respectively. Favorable performance in terms of $B_1$ measurements for a TEM coil compared to a shielded birdcage coil was also experimentally demonstrated at 4 T [4].

Finally, advantages of the TEM resonator over the traditional birdcage design are expected to become more apparent for shorter RF-wavelengths at even higher field strengths ($B_0 \geq 4$ T). This is due to the fact that in theory, the TEM circuit eliminates radiation losses, which increase as the fourth power of frequency [4]. This coil design lends itself to the development of TEM coil arrays to further improve the SNR and to enable the use of parallel imaging techniques, while retaining the benefit of increased $(\gamma \cdot B_1/2\pi)$.

In summary, at the clinical field strength of $B_0 = 3$ T higher SNR values in phantom and human brain images were measured using the TEM coil as compared to the CP coil. In selected areas, these values were close to those obtained with the 12-channel array coil, with which the highest SNR was achieved for human data. On the other hand, as expected, increased image intensity variations and RF-power deposition were noted for the 12-channel coil compared to the other two coils. In terms of $B_1^+$ excitation fields, the TEM and the CP coils achieved similar results and higher effective flip angles than the 12-channel coil/body coil setup. It is concluded that, if these three or a similar set of coils is available, the various advantages and disadvantages of the individual coils suggest that coil selection is determined by the application at hand, e.g., depending on whether the highest possible SNR or largest $B_1^+$ field strength is required.

**Acknowledegments** The authors would like to thank Martin Hergt for helpful discussions and the reviewers for their valuable comments.

## References


1. Hoult DI (2000) Sensitivity and power deposition in a high-field imaging experiment. J Magn Reson Imaging 12:46–67
2. Vaughan JT, Hetherington HP, Otu JO, Pan JW, Pohost GM (1994) High frequency volume coils for clinical NMR imaging and spectroscopy. Magn Reson Med 32:206–218
3. Zhang X, Ugurbil K, Chen W (2001) Microstrip RF surface coil design for extremely high-field MRI and spectroscopy. Magn Reson Med 46:443–450
4. Vaughan JT, Adriany G, Garwood M, Yacoub E, Duong T, DelaBarre L, Andersen P, Ugurbil K (2002) Detunable transverse electromagnetic (TEM) volume coil for high-field NMR. Magn Reson Med 47:990–1000
5. Vaughan JT, Garwood M, Collins CM, Liu W, DelaBarre L, Adriany G, Andersen P, Merkle H, Goebel R, Smith MB et al (2001) 7T vs. 4T: RF power, homogeneity, and signal-to-noise comparison in head images. Magn Reson Med 46:24–30
6. Avdievich NI, Hetherington HP (2004) 4 T actively detunable transmit/receive transverse electromagnetic coil and 4-channel receive-only phased array for (1)H human brain studies. Magn Reson Med 52:1459–1464
7. Zhang X, Ugurbil K, Chen W (2003) A microstrip transmission line volume coil for human head MR imaging at 4T. J Magn Reson 161:242–251
8. Hayes CE, Edelstein WA, Schenck JF, Mueller OM, Eash M (1985) An efficient, highly homogeneous radiofrequency coil for whole-body NMR imaging at 1.5 T. J Magn Reson 63:622–628
9. Roemer PB, Edelstein WA, Hayes CE, Souza SP, Mueller OM (1990) The NMR phased array. Magn Reson Med 16:192–225
10. Alecci M, Collins CM, Smith MB, Jezzard P (2001) Radio frequency magnetic field mapping of a 3 Tesla birdcage coil: experimental and theoretical dependence on sample properties. Magn Reson Med 46:379–385
11. Ohliger MA, Sodickson DK (2006) An introduction to coil array design for parallel MRI. NMR Biomed 19:300–315
12. Liu W, Collins CM, Delp PJ, Smith MB (2004) Effects of end-ring/shield configuration on homogeneity and signal-to-noise ratio in a birdcage-type coil loaded with a human head. Magn Reson Med 51:217–221
13. Ibrahim TS, Mitchell C, Schmalbrock P, Lee R, Chakeres DW (2005) Electromagnetic perspective on the operation of RF coils at 1.5–11.7 Tesla. Magn Reson Med 54:683–690
14. Wang C, Shen GX (2006) B1 field, SAR, and SNR comparisons for birdcage, TEM, and microstrip coils at 7T. J Magn Reson Imaging 24:439–443
15. Tropp J (2002) Dissipation, resistance, and rational impedance matching for TEM and birdcage resonators. Concepts Magn Reson B 15:177–188
16. Wiggins GC, Potthast A, Triantafyllou C, Wiggins CJ, Wald LL (2005) Eight-channel phased array coil and detunable TEM volume coil for 7 T brain imaging. Magn Reson Med 54:235–240
17. Hoult DI (2000) The principle of reciprocity in signal strength calculations - A mathematical guide. Concepts Magn Reson 12:173–187
18. Insko EK, Bolinger L (1993) Mapping of the radiofrequency field. J Magn Reson, Ser A 103:82–85
19. Stollberger R, Wach P (1996) Imaging of the active B1 field in vivo. Magn Reson Med 35:246–251
20. Jenkinson M, Bannister P, Brady M, Smith S (2002) Improved optimization for the robust and accurate linear registration and motion correction of brain images. Neuroimage 17:825–841
21. Collins CM, Yang QX, Wang JH, Zhang X, Liu H, Michaeli S, Zhu XH, Adriany G, Vaughan JT, Anderson P et al (2002) Different excitation and reception distributions with a single-loop transmit-receive surface coil near a head-sized spherical phantom at 300 MHz. Magn Reson Med 47:1026–1028
22. Wang J, Qiu M, Yang QX, Smith MB, Constable RT (2005) Measurement and correction of transmitter and receiver induced nonuniformities in vivo. Magn Reson Med 53:408–417
23. Collins CM, Liu W, Schreiber W, Yang QX, Smith MB (2005) Central brightening due to constructive interference with, without, and despite dielectric resonance. J Magn Reson Imaging 21:192–196